Plane Wave Imaging Techniques for Immersion Testing of Components with Non-Planar Surfaces

Rosen K. Rachev, Paul D. Wilcox, Alexander Velichko, and Kevin L. McAughey

***Abstract*—Plane Wave Imaging (PWI) is an ultrasonic array imaging technique used in non-destructive testing, that has been shown to yield high resolution with few transmissions. Only a few published examples are available of PWI of components with non-planar surfaces in immersion. In these cases, inspections were performed by adapting the transmission delays in order to produce a plane wave inside the component. This adaptation requires prior knowledge of the component geometry and position relative to the array. The current paper proposes a new implementation, termed PWI Adapted in Post-Processing (PWAPP), which has no such requirement. In PWAPP the array emits a plane wave as in conventional PWI. The captured data is input into two post-processing stages. The first reconstructs the surface of the component, the latter images inside of it by adapting the delays to the distortion of the plane waves upon refraction at the reconstructed surface. Simulation and experimental data are produced from an immersed sample with a concave front surface and artificial defects. These are processed with conventional and surface corrected PWI. Both algorithms involving surface adaptation produced nearly equivalent results from the simulated data, and both outperform the non-adapted one. Experimentally, all defects are imaged with Signal-to-Noise Ratio (SNR) of at least 31.8 and 33.5 dB for respectively PWAPP and PWI adapted in transmission, but only 20.5 dB for conventional PWI. In the cases considered, reducing the number of transmissions below the number of array elements shows PWAPP maintains its high SNR performance down to number of firings equivalent to a quarter of the array elements. Finally, experimental data from a more complex surface specimen is processed with PWAPP resulting in detection of all scatterers and producing SNR comparable to that of the Total Focusing Method.**

***Index Terms*—ultrasound, non-destructive evaluation, plane wave imaging, immersion testing, signal processing, complex geometry.**

I. Introduction

MOST industries have already adopted the use of ultrasonic phased arrays instead of monolithic transducers for non-destructive evaluation (NDE) [1]–[3]. Phased arrays are much more versatile as they allow different inspections to be undertaken with the same equipment, potentially providing higher sensitivity and better coverage. More recently, ultrasonic phased array imaging has been established as a preferred and more intuitive processing of acquired inspection data [4]. The Total Focusing Method (TFM) is described as the "gold standard" for ultrasonic imaging [5], [6]. This technique utilises the full response of an array. The full matrix capture (FMC) of data corresponding to the time domain signals from all transmit-receive element pairs is captured and post-processed to form the final image. The advantage of the approach over conventional beamforming techniques is that the image is produced by focusing in transmission and reception at every pixel, achieving the optimal spatial resolution.

A challenge for the ultrasonic NDE industry is that structures of interest often have few planar surfaces. There are two approaches to transmit ultrasound through a complex surface using a phased array [7]. The first is to match the array geometry to the component allowing direct coupling and transmission [8]–[11]. However, employing a flexible phased array is often a sacrifice in robustness and the use of a bespoke one adds significant costs. The second approach is to introduce an intermediary medium between the array and the component. This can be a perspex wedge [12], a liquid-filled bag [13] or a liquid bath in which the whole inspection setup is immersed [14]–[16].

The benefit of the immersion approach is that it allows inspection of complex profile components without requiring prior knowledge of their geometries [17], [18]. Instead, those geometries are measured directly from the acquired ultrasonic data through post-processing with a surface reconstruction technique [19], [20]. Hence, once the geometry of a specimen is known (shapes and positions of the front and back surfaces), the same phased array data can be used to form multiple images inside of it [21]. The images correspond to the views produced with the different combinations of propagation modes [22], [23]. For example, during an immersion test with a single data acquisition stage, direct mode imaging in the couplant can be used for reconstruction of the front surface, a second direct mode longitudinal image inside the specimen can reveal the back surface, which allows a final shear wave half-skip image sensitive to back surface-breaking cracks to be formed [24].

TFM, while offering clear performance advantages, requires a large number of transmissions, equal to at least the number of array elements. Also, the post-processing of the large FMC data set itself is computationally intensive. These drawbacks make it difficult to apply TFM in cases where a limit is imposed on the capture time (e.g. pipeline in-line inspections [25]), or high frame-rates are required (medical imaging). Various adaptations to the algorithm are present in the literature which reduce the required number of firings through sparsity of the collected data [26]–[29]. Such implementations result in compromised resolution in comparison to TFM. Furthermore, their performance depends on imaging parameters which have been tailored to a specific inspection and need to be optimised differently if the inspection scenario changes.

R. Rachev is with the Department of Mechanical Engineering, University of Bristol, Bristol BS8 1TR, U.K., and also with Baker Hughes, Cramlington, NE23 1WW, U.K. (e-mail: rr12520@.bristol.ac.uk).

P. Wilcox and A. Velichko are with the Department of Mechanical Engineering, University of Bristol, Bristol BS8 1TR, U.K.

At the time of this research K. McAughey was with Baker Hughes, Cramlington, NE23 1WW, U.K

Manuscript received August 13, 2019; revised December 5, 2019.

Recently, another imaging method termed Plane Wave Imaging (PWI) [30]–[32] was proposed. It addresses the speed of acquisition issue without requiring precise tuning to a specific inspection. The principle is to transmit plane waves at different angles inside the inspection region of interest. On reception, all elements record in parallel. This allows dynamic reception focusing in post-processing at each pixel in the image. An advantage of this technique is that higher power is input into the component due to the transmission with multiple elements rather than a single one. More importantly, PWI is shown to yield images of comparable resolution to TFM with significantly fewer acquisition cycles [33]. The work presented in [32] investigates the PWI performance in immersion scenarios as well as imaging in different modalities. An extension to this work is presented in [34], which addresses PWI through complex surfaces. The authors apply appropriate time delays to the array elements in order to produce a plane wave inside the component rather than in the couplant. This is a common method to compensate distortions of the ultrasound beam caused by a non-planar surface geometry [35] and allows the formation of images of comparable quality to those formed through a planar surface. The drawback of this approach is the requirement that the front surface profile and transducer orientation with respect to it are known prior to emitting the transmitted wavefront.

This paper proposes an alternative PWI approach which does not require prior knowledge of the inspection configuration, but forms images of comparable sensitivity to the ones produced by the technique in [34]. In the proposed approach, a plane wave is transmitted inside the couplant, without accounting for the front surface geometry. The front surface profile can be reconstructed in post-processing directly from the received signals. During the image formation within the specimen, the plane wave distortion caused by propagation through the reconstructed interface is taken into consideration. This information is used to map the path between the imaged pixel and the part of the array the signal originates from. The mapping is similar to the one performed in Pixel-Based Beamforming techniques [36] proposed for medical imaging with focused beams.

In Section II, the different PWI techniques are outlined. Sections III and IV present the model used to generate ultrasonic data from a reflector in an immersed pipe-like component and the results the different PWI algorithms output when applied to that data. Section V shows experimental results with the PWI algorithms used on data collected from immersed components with concave and sinusoidal surfaces. Those are assessed in terms of number of plane wave firings and compared to TFM.

II. Methods

All immersion testing requires prior knowledge or measurements of the specimen's geometry and location with respect to the phased array in order to process the acquired ultrasonic array data into meaningful information about the structural integrity of the component. A detailed discussion on the different approaches to obtain the front surface reconstruction is beyond the scope of this paper. In the algorithms presented it is assumed that an accurate interface measurement has been extracted. The focus is instead on how to adapt the transmission or post-processing to that surface, in order to form a PWI of the specimen in immersion. The different approaches to cancel the distortion of the plane waves upon transmission from the couplant into the specimen along with their underlying assumptions are discussed in the following subsections.

A. PWI with No Adaptation (PWNA)

In PWI with No Adaptation (PWNA), the interface geometry at the plane wave incidence is considered planar causing no distortion to the wave refracted through it. This significantly simplifies the image formation. A diagram illustrating the assumed ray paths is shown in Figure 1a and the procedure to implement it is presented in the following paragraphs.

Let the q-th plane wave be transmitted in the direction defined by the unit vector $\hat{\boldsymbol{I}}_q$, and the incident point of the plane wave centre onto the component front surface be $\boldsymbol{s}_q$. Then, the distance $\zeta_q^{(1)}$ from the array centre $\boldsymbol{a}_c$ to this front surface crossing point is:

$$\zeta_q^{(1)} = (\boldsymbol{s}_q - \boldsymbol{a}_c) \cdot \hat{\boldsymbol{I}}_q \tag{1}$$

For image formation purposes, under the PWNA scheme, the insonified portion of the front surface is assumed planar. Its normal is approximated by the surface normal vector $\boldsymbol{n}_q$ at the central incident point $\boldsymbol{s}_q$. Therefore, the transmitted plane wave is assumed to stay planar after refraction through the interface. This is illustrated in Figure 1a. The approximation is valid when the ratio of the plane wave width to surface curvature radius is small. Using Snell's Law [37] the direction of the refracted central ray (defined by the unit vector $\hat{\boldsymbol{R}}_q$) of the plane wave inside the specimen can be expressed as:

$$\hat{\boldsymbol{R}}_q = \eta_{12}\hat{\boldsymbol{I}}_q + \nu_q \hat{\boldsymbol{n}}_q \tag{2}$$

where

$$\eta_{12} = \frac{c_2}{c_1} \quad \text{and} \quad \nu_q = \eta_{12} C_q - \sqrt{1 + \eta_{12}^2 (C_q^2 - 1)} \tag{3}$$

c_1 and c_2 are the velocities in respectively the couplant and specimen, and C_q is the cosine of the angle between the surface normal $\hat{\boldsymbol{n}}_q$ and the plane wave central ray unit vector $\hat{\boldsymbol{I}}_q$:

$$C_q = -\hat{\boldsymbol{I}}_q \cdot \hat{\boldsymbol{n}}_q \tag{4}$$

Let the coordinates of an imaged pixel be $\boldsymbol{r}$. When the plane wave front passes through $\boldsymbol{r}$, the distance traveled by the plane wave inside the specimen is $\zeta_q^{(2)}(\boldsymbol{r})$. This is equivalent to the component of the vector connecting the central incidence point $\boldsymbol{s}_q$ to the imaged point $\boldsymbol{r}$ in the direction of the refracted plane wave $\hat{\boldsymbol{R}}_q$:

$$\zeta_q^{(2)}(\boldsymbol{r}) = (\boldsymbol{r} - \boldsymbol{s}_q) \cdot \hat{\boldsymbol{R}}_q \tag{5}$$

Then, the outbound travel time from the phased array centre to the imaged pixel point $\boldsymbol{r}$ is:

$$T_q^{(out)}(\boldsymbol{r}) = \frac{\zeta_q^{(1)}}{c_1} + \frac{\zeta_q^{(2)}(\boldsymbol{r})}{c_2} \tag{6}$$

This article has been accepted for publication in a future issue of this journal, but has not been fully edited. Content may change prior to final publication. Citation information: DOI 10.1109/TUFFC.2020.2969083, IEEE Transactions on Ultrasonics, Ferroelectrics, and Frequency Control

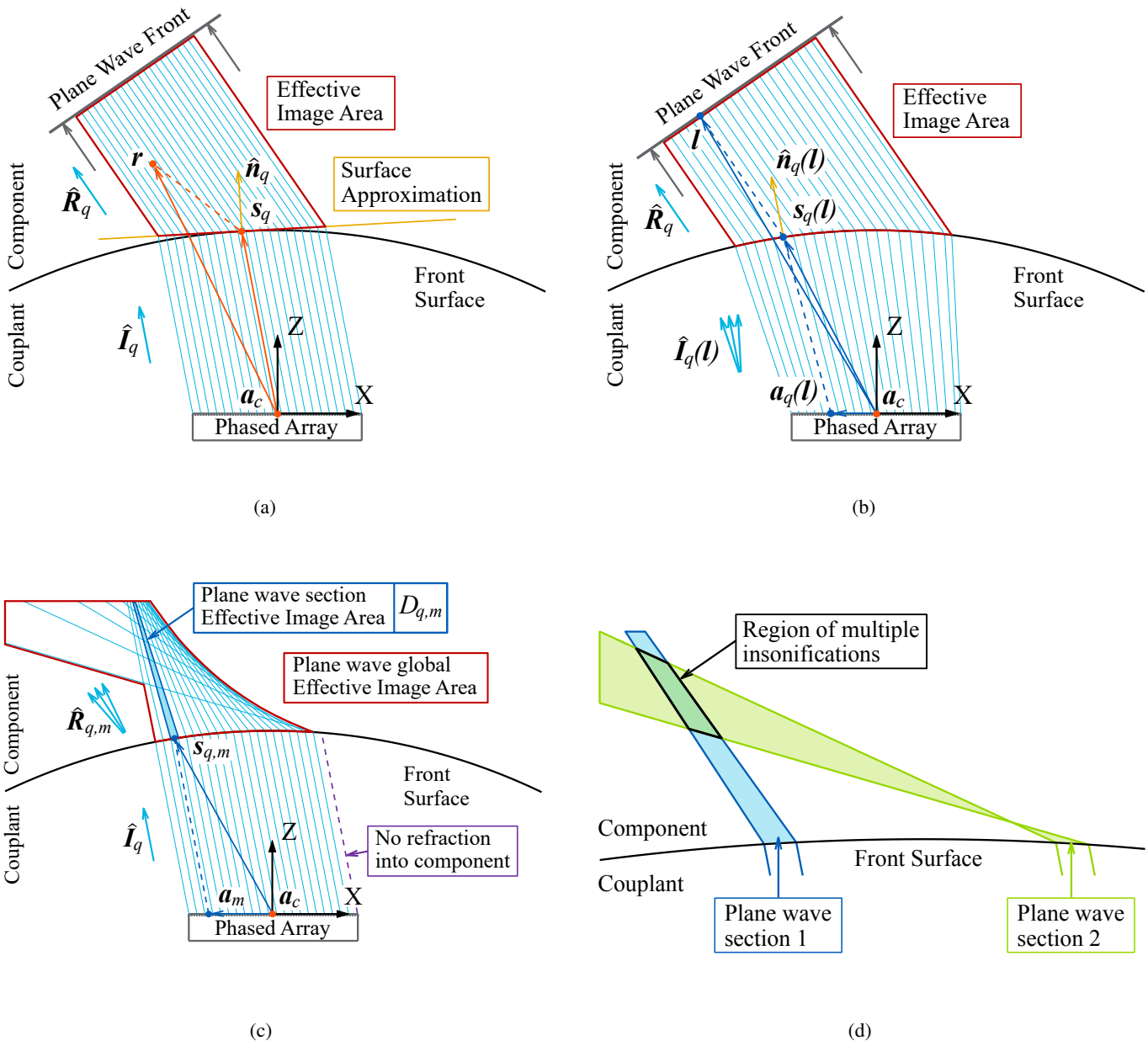

Fig. 1: Assumed plane wave outbound (transmission) ray paths for refraction from water into steel according to different variants of the PWI algorithm: (a) PWI with No Adaptation (PWNA); (b) PWI Adapted in Transmission (PWAT); (c) PWI Adapted in Post-Processing (PWAPP); (d) PWAPP zoomed on a region insonified multiple times by a single plane wave.

The focusing on reception is the same as for the TFM algorithm [6] and is independent of the transmitted q-th plane wave characteristics. To obtain the appropriate time delays, the coordinates of the refraction points $\boldsymbol{s}_j(\boldsymbol{r})$ on the interface are calculated. Those correspond to the set of points, through which the rays, connecting each imaged pixel $\boldsymbol{r}$ to each receive phased array element j (with coordinates $\boldsymbol{a}_j$) have to pass to satisfy Snell's law. The inbound delay is therefore:

$$T_j^{(in)}(\boldsymbol{r}) = \frac{|\boldsymbol{s}_j(\boldsymbol{r}) - \boldsymbol{a}_j|}{c_1} + \frac{|\boldsymbol{r} - \boldsymbol{s}_j(\boldsymbol{r})|}{c_2} \tag{7}$$

For an A-scan $g_{q,j}$ corresponding to the q-th transmitted wave and j-th receiving array element, recorded such that the plane wave front passes through the array centre at time 0, the total delay applied to calculate the intensity at a pixel $\boldsymbol{r}$ is:

$$T_{q,j}(\boldsymbol{r}) = T_q^{(out)}(\boldsymbol{r}) + T_j^{(in)}(\boldsymbol{r}) \tag{8}$$

As suggested by [32] the imaging is only applied within the effective image area D_q (the sub-region insonified by the corresponding q-th plane wave, shown in red in Figure 1a). The final image intensity $I(\boldsymbol{r})$ at a point $\boldsymbol{r}$ is the summation:

$$I(\boldsymbol{r}) = \sum_{q=1}^{Q} \left(\kappa_q(\boldsymbol{r}) \sum_{j=1}^{N} g_{q,j}(T_{q,j}(\boldsymbol{r})) \right) \tag{9}$$
$$\text{where } \kappa_q(\boldsymbol{r}) = 1 \text{ if } \boldsymbol{r} \in D_q$$
$$\text{and } \kappa_q(\boldsymbol{r}) = 0 \text{ if } \boldsymbol{r} \notin D_q$$

where Q is the number of transmitted plane waves and N is the number of elements in the phased array.

B. PWI Adapted in Transmission (PWAT)

When the radius of the front surface curvature is small, the assumption that a transmitted into the couplant plane wave remains planar after refraction through the interface is no longer appropriate. An alternative approach is to apply transmit delays onto the elements to produce a plane wave inside the specimen [34]. The idea is illustrated in Fig. 1b. This requires prior knowledge of the component surface. Additionally, it leads to a wave front in the couplant which is not planar. However, this is not a drawback since focusing and imaging in the couplant is rarely of interest once the component surface is established. The algorithm to calculate the adapted transmission delays and consequently image the specimen is presented below.

Let the q-th plane wave be transmitted into the specimen in a direction defined by the unit vector $\hat{\boldsymbol{R}}_q$. Firstly, the beam-forming time delay $\Delta T_{q,i}^{(AT)}$ required at the i-th transmit phased array element to form such a plane wave has to be calculated. This is done through ray tracing from a plane wave front inside the specimen, through the interface, and back to the phased array. The plane wave front is perpendicular to the plane wave propagation direction and is shown in grey in Figure 1b. Let $\boldsymbol{l}$ be a point on the plane wave front. A ray originating from $\boldsymbol{l}$ is constructed in the direction $\hat{\boldsymbol{R}}_q$. The crossing point $\boldsymbol{s}_q(\boldsymbol{l})$ of the ray with the front surface and the front surface normal $\boldsymbol{n}_q(\boldsymbol{l})$ at this crossing are calculated. Note that in the PWI Adapted in Transmission (PWAT) algorithm, the full set of front surface crossing points and normals are used, rather than just the central ray one, resulting in the dependency on the ray point of origin $\boldsymbol{l}$. Then, Snell's law (eq. 2) is applied for refraction from the specimen into the couplant. Hence, the front surface incident ray direction $\hat{\boldsymbol{I}}_q(\boldsymbol{l})$ that produces the refracted $\hat{\boldsymbol{R}}_q$ is calculated as:

$$\hat{\boldsymbol{I}}_q(\boldsymbol{l}) = \eta_{21}\hat{\boldsymbol{R}}_q + \nu_q(\boldsymbol{l})\hat{\boldsymbol{n}}_q(\boldsymbol{l}) \tag{10}$$

At this stage the rays $\hat{\boldsymbol{I}}_q(\boldsymbol{l})$ are no longer parallel and have different gradients/angles depending on which part of the plane wave front ($\boldsymbol{l}$) they propagate to. This is observable in the rays connecting the array to the front surface in Fig. 1b. Similarly to the previous stage, the crossing points $\boldsymbol{a}_q(\boldsymbol{l})$ of the $\boldsymbol{I}_q(\boldsymbol{l})$ rays with the phased array surface can be calculated. The travel time from the array to the plane wave front along the rays can therefore be calculated with respect to arriving location onto the plane wave front ($\boldsymbol{l}$):

$$T_q^{(tt)}(\boldsymbol{l}) = \frac{|\boldsymbol{s}_q(\boldsymbol{l}) - \boldsymbol{a}_q(\boldsymbol{l})|}{c_1} + \frac{|\boldsymbol{l} - \boldsymbol{s}_q(\boldsymbol{l})|}{c_2} \tag{11}$$

For a smooth surface the rays connect a single point onto the plane wave front with a single point within the phased array aperture. Hence, the calculated travel times function $T_q^{(tt)}(\boldsymbol{l})$ can be redefined as $T_q^{(tt)}(\boldsymbol{a})$ in terms of position onto the array surface $\boldsymbol{a}$. In practice, linear interpolation is used on the values from the redefined function to compute the travel time $T_q^{(tt)}(\boldsymbol{a}_i)$ for the i-th array element.

Similarly to the previous algorithm, the travel time corresponding to the centre of the array to the plane wave front is taken as a reference and the delay/forwarding times are calculated with respect to it. This allows the PWNA post-processing algorithm to be applied to the PWAT data without any major adjustments. The beam forming delay $\Delta T_{q,i}^{(AT)}$ for the i-th transmit element is calculated as:

$$\Delta T_{q,i}^{(AT)} = T_q^{(tt)}(\boldsymbol{a}_i) - T_q^{(tt)}(\boldsymbol{a}_c) \tag{12}$$

Physically, signals cannot be transmitted with negative delays (forwarding), therefore a constant time offset $T^{(os)}$ is added such that $T^{(os)} + T_{q,i}^{(AT)} \geq 0$. After collection time-trace data are shifted so that time 0 corresponds to the plane wave front passing through the array centre. Also note that since the transmit and receive apertures are the same, the indices i and j are used to specify an element from the same set of phased array elements. However, the first indicates the element is transmitting, while the latter shows the element is receiving.

Data collected in the aforementioned manner are then post-processed. The central ray path is calculated in exactly the same manner as for the PWNA algorithm. The distance from the array to the plane wave front along the central ray, and hence the outbound time delay is given by equation 6. The inbound and total delays are given by equations 7 and 8. The imaging algorithm is applied to the effective image area D_q. This sub-region is shown in red in Figure 1b. It is similar to the PWNA one, except in PWAT the real front surface of the component and the actual insonified sub-region are used rather than approximations. The final image is a summation of the images for each individual plane wave firing given by equation 9.

C. PWI Adapted in Post-Processing (PWAPP)

In some applications the geometry of the inspected component is not known in advance and there is no opportunity to perform multiple scans to firstly reconstruct the surfaces and then adapt the transmissions. The algorithm proposed in this section does not require the exact inspection configuration as an input, since it does not rely on altering the transmission patterns. Instead, the method utilises multiple post-processing stages applied to the same data set to firstly reconstruct the surface of the component and then adapt the ray tracing of the PWI to an assumed distortion profile of the plane waves. This section provides a detailed explanation of the latter part of the algorithm: the PWI Adapted in Post-Processing (PWAPP).

The post-processing is applied to the same set of data captured for the PWNA. The first step is to calculate the outbound delay from the array to an imaged point $\boldsymbol{r}$. Let the q-th plane wave be transmitted inside the couplant in a direction defined by the unit vector $\hat{\boldsymbol{I}}_q$. For the purpose of post-processing this plane wave is split into M smaller plane waves of the same width in the couplant. These are represented schematically as the regions between the light blue rays in Fig. 1c. If M is large, the plane wave sections behave under the assumptions used for the PWNA algorithm. Therefore, the outbound time delay $\tau_{q,m}^{(out)}(\boldsymbol{r})$ with respect to the plane wave

section centre is expressed similarly to the one in equation 6:

$$\tau_{q,m}^{(out)}(\boldsymbol{r}) = \frac{(\boldsymbol{s}_{q,m} - \boldsymbol{a}_m) \cdot \hat{\boldsymbol{I}}_q}{c_1} + \frac{(\boldsymbol{r} - \boldsymbol{s}_{q,m}) \cdot \hat{\boldsymbol{R}}_{q,m}}{c_2} \quad (13)$$

where the m-th plane wave part originates from the centered at $\boldsymbol{a}_m$ phased array sub-aperture, $\boldsymbol{s}_{q,m}$ is the interface crossing point with the central ray from $\boldsymbol{a}_m$ in the direction $\hat{\boldsymbol{I}}_q$, and $\hat{\boldsymbol{R}}_{q,m}$ is the unit vector direction of the refracted inside the component central ray following Snell's Law (eq. 2). It is noted the rays inside the specimen are no longer parallel and the wave is not planar, hence the m dependency in $\hat{\boldsymbol{R}}_{q,m}$. This can also be observed in Figure 1c. The time delay $\mathcal{T}_{q,m}^{(out)}(\boldsymbol{r})$ from equation 13 needs to be adjusted to a unified global point rather than the local sub-aperture centres $\boldsymbol{a}_m$. Hence, the final PWAPP outbound time delay $T_{q,m}^{(out)}(\boldsymbol{r})$ w.r.t. the phased array centre $\boldsymbol{a}_c$ is:

$$T_{q,m}^{(out)}(\boldsymbol{r}) = \frac{-\hat{\boldsymbol{I}}_q(\boldsymbol{a}_m - \boldsymbol{a}_c)}{c_1} + \tau_{q,m}^{(out)}(\boldsymbol{r}) \quad (14)$$

A few intricacies are present in the way those delays are applied to the domain to form the final image. Firstly, to model the true behaviour of the plane wave M should be infinitely large. However, in practice sufficient representation can be obtained with a relatively few sections. The optimal value in terms of accurate representation against computational efficiency is dependent on the phased array pitch, frequency and component geometry. The relationship is not explored in this paper. Instead, the problem is simplified to selecting M such that the adjacent refracted rays (light blue in the component half-space Fig. 1c) are near parallel to each other. The value of $M = 2N - 1$ is found sufficiently large to meet this criteria. Secondly, at some extreme firing angles, or for complex surfaces, parts of the transmitted from the array plane wave could be incident onto the media interface at angles above the critical. This means a portion of the plane wave will not refract into the component. However, the rest of it can still be used for imaging. In the imaging algorithm, plane wave sections between rays incident onto the interface above the critical angle are ignored. The scenario is also illustrated in Fig. 1c, where a ray is not constructed inside the specimen from the rightmost element of the phased array (dashed purple ray). Furthermore, instead of creating a single global effective image area D_q for a plane wave q, multiple ones $D_{q,m}$ are formed corresponding to the areas insonified by each plane wave section, bounded by the front surface and the end of the domain. The equivalent plane wave global effective image area (or the total area that can be imaged by a single plane wave transmission) is the combined area covered by all sections of the transmitted plane wave. The section and global areas are illustrated in Fig. 1c. A benefit of this utilisation is in handling rays which cross and stack on top of each other. An example of the phenomenon is observed in Figure 1d, where the pixels in the black quadrilateral are in the effective image areas of two plane wave sections. These pixels are insonified multiple times by the same transmission at different travel times through refractions from different positions onto the front surface. The separate post-processing of the pixels in multiple imaging regions will ensure consistent focusing results.

The inbound delays are the same as for the previous two algorithms (eq. 7). The total delay is given by eq. 8. The final image is the summation of the images of each of the M sub-regions $D_{q,m}$ for each individual plane wave firing q:

$$I(\boldsymbol{r}) = \sum_{q=1}^{Q} \left(\sum_{m=1}^{M} \kappa_{q,m}(\boldsymbol{r}) \sum_{j=1}^{N} g_{q,j}(T_{q,j}(\boldsymbol{r})) \right) \quad (15)$$
$$\text{where } \kappa_{q,m}(\boldsymbol{r}) = 1 \text{ if } \boldsymbol{r} \in D_{q,m}$$
$$\text{and } \kappa_{q,m}(\boldsymbol{r}) = 0 \text{ if } \boldsymbol{r} \notin D_{q,m}$$

III. Modelling

The aforementioned algorithms will be compared in scenarios close to actual industrial inspections. In order to efficiently cover a wide range of inspection configuration parameters a simulation has been designed as the initial step in this comparison. An advantage of using simulated instead of experimental data is the effects of noise and media speed of sound inaccuracies will not be present. An omni-directional scatterer is modelled under a circular concave surface in immersion. This setup is close to the real world inspections of various types of defects in pipes (e.g. porosity, pitting, cracks, etc.). A 2-Dimensional (2D) forward model is used and only the longitudinal-longitudinal direct mode paths to the scatterer are simulated ignoring all reflections from the component's geometry. The model outputs the FMC response of the phased array to the reflector. The different steps to produce the simulation are presented in this section.

Firstly, the signal output from the phased array elements is modelled. It is a five cycle, Hanning windowed (-6 dB bandwidth of 50%) tone burst with a frequency spectrum $\Phi(\omega)$. This signal has to be propagated along the ray paths from an element to the defect and back. A transmit ray path from an element at $\boldsymbol{a}_i$ to the scatterer at $\boldsymbol{p}$ is illustrated in Figure 2a. The front surface refraction point $\boldsymbol{s}_i$ on this path is calculated using Fermat's minimum time principle. Therefore, the travel distances in the couplant $L_i^{(1)}$ and the concave specimen $L_i^{(2)}$ as well as the propagation time T_i from an element i to the scatterer are:

$$L_i^{(1)} = |\boldsymbol{s}_i - \boldsymbol{a}_i| \quad \text{and} \quad L_i^{(2)} = |\boldsymbol{p} - \boldsymbol{s}_i| \quad (16)$$

$$T_i = \frac{L_i^{(1)}}{c_1} + \frac{L_i^{(2)}}{c_2} \quad (17)$$

To simulate the propagation, in addition to delaying, amplitude scaling is applied to the signal. This scaling is introduced through the coefficients for phased array element directivity, beam spreading and partial transmission [38]. The 2D element directivity function is defined in terms of amplitude w.r.t. ray angle from the phased array normal in the steering plane. Let this angle be ψ_i (shown in Figure 2a). Therefore, the 2D directivity function F_i for an element i is:

$$F_i = \text{sinc}\left(\frac{\pi b \sin\psi_i}{\lambda}\right) \quad (18)$$

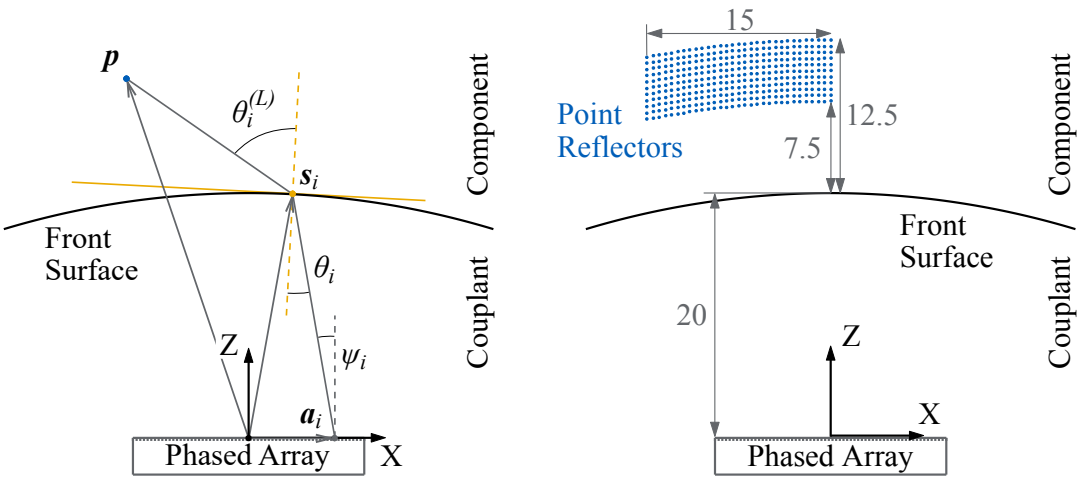

Fig. 2: Simulation configuration of the scatterers under a concave surface: (a) Ray path from transmit element i to a scatterer at $\boldsymbol{p}$; (b) Phased array, front surface and full set of point scatterers (dimensions in mm).

where b is the element width and λ is the central frequency. The beam-spread function A_i describes the loss in amplitude due to beam spread in both media (without contributions from attenuation or partial transmission). For a transmission from the couplant into the specimen, denoted with a superscript $^{(12)}$, this is as follows:

$$A_i^{(12)} = \sqrt{\beta_i^{(12)}} \frac{1}{\sqrt{\beta_i^{(12)} L_i^{(1)} + L_i^{(2)}}} \tag{19}$$

$$\beta_i^{(12)} = \frac{c_1^2/c_2^2 - \sin^2\theta_i}{(c_1/c_2)\cos^2\theta_i} \tag{20}$$

where θ_i is the angle the incident ray forms with the pipe surface normal. It should be noted ψ_i and θ_i are different since the pipe front surface is not planar and hence not parallel to the phased array surface. This is also observed in Fig. 2a. Finally, the partial transmission coefficients between liquid and solid media are given by [39]. For an incident longitudinal wave in a liquid and a refracted longitudinal wave in the solid the formula is:

$$V_i^{(12)} = \frac{2}{N_i} \frac{c_1 \rho_1}{c_2 \rho_2} \cos 2\theta_i^{(T)} \tag{21}$$

$$N_i = \frac{c_3^2}{c_2^2} \sin 2\theta_i^{(L)} \sin 2\theta_i^{(T)} + \cos^2 2\theta_i^{(T)} + \frac{\rho_1 c_1}{\rho_2 c_2} \frac{\cos\theta_i^{(L)}}{\cos\theta_i} \tag{22}$$

where c_3 is the shear wave speed in the solid, $\theta_i^{(L)}$ and $\theta_i^{(S)}$ are respectively the angles of the longitudinal and transverse rays refracted into the solid, ρ_1 and ρ_2 are the densities in the liquid couplant and solid pipe specimen. Equations 16 to 22 are sufficient to simulate the wave behaviour on the outbound paths (from the phased array elements to the defect). Almost all coefficients for the inbound paths can be calculated using the same formulas, through substituting the dependence on transmit element i to dependence on receive element j. The exceptions are the beam spreading $A_j^{(21)}$ and partial transmission $V_j^{(21)}$, since the boundary switches from liquid-solid to solid-liquid. Those are given by:

$$A_j^{(21)} = \sqrt{\beta_j^{(21)}} \frac{1}{\sqrt{L_j^{(1)} + \beta_j^{(21)} L_j^{(2)}}} \tag{23}$$

$$V_j^{(21)} = \frac{2}{N_j} \frac{\cos\theta_j^{(L)} \cos 2\theta_j^{(T)}}{\cos\theta_j} \tag{24}$$

where $\beta_j^{(21)} = 1/\beta_j^{(12)}$. Therefore, the resulting spectrum $H_{i,j}(\omega)$ for a transmit-receive pair of elements i-j is:

$$H_{i,j}(\omega) = F_i F_j A_i^{(12)} A_j^{(21)} V_i^{(12)} V_j^{(21)} \Phi(\omega) e^{-\iota\omega(T_i+T_j)} \tag{25}$$

where the imaginary unit is denoted ι to avoid confusion with the transmit and receive element indices i and j. The final time domain signals $h_{i,j}(t)$ are the inverse Fourier transform of the $H_{i,j}(\omega)$ spectra.

IV. Modelling Results and Discussion

The model has been used to generate FMC data sets with input parameters as defined in Table I. The phased array parameters have been specified to simulate a commercial probe manufactured by Imasonic, Besancon, France. Figure 2b defines the coordinate system and the geometry of the simulated setup, including the full set of defects. The location of these simulated scatterers is defined in terms of depth under the front surface and lateral position (x-coordinate) away from the centreline of the ultrasonic array. The depths range from 7.5 mm to 12.5 mm at every 0.5 mm, while the x-coordinates are from -15 to 0 mm at every 0.5 mm. Note that reflectors are simulated only on one side of the phased array centreline since the setup is symmetric. Front surface radii from 50 mm to 300 mm are examined.

The simulation algorithm outputs ultrasonic data $h(t)$ in FMC format. The techniques presented in Section II require

TABLE I: Inspection setup parameters.

Parameter	Value
Phased array properties	
Centre frequency	5 MHz
Sample frequency	50 MHz
Number of elements	64
Element pitch	0.3 mm
Element size	0.28 mm
Materials properties	
Couplant density	1000 kg/m^3
Couplant speed of sound	1480 m/s
Specimen density	8000 kg/m^3
Specimen longitudinal wave speed	5673 m/s
Specimen shear wave speed	3086 m/s

input data in plane wave format (time traces w.r.t wave transmission q and receiving element j). Therefore, the first post-processing step is to convert the FMC data $h(t)$ into plane wave data format $g(t)$. This is implemented through a time-shift and summation. The centre of the phased array is taken as a reference point and its delay is 0. For PWNA and PWAPP, the advance/delay $\Delta T_{q,i}^{(NA)}$ on the i-th element to produce the q-th plane wave is given by:

$$\Delta T_{q,i}^{(NA)} = \frac{-\hat{\boldsymbol{I}}_q(\boldsymbol{a}_i - \boldsymbol{a}_c)}{c_1} \tag{26}$$

whereas for PWAT the beam formation time shift $\Delta T_{q,i}^{(AT)}$ is given in equation 12. Either way, the time shift $\Delta T_{q,i}$ is applied along the FMC columns (w.r.t. different transmitters i), the signals in each of which are then summed. Hence, the q-j time trace entry in the plane wave data is synthesised from the FMC according to the equation:

$$g_{q,j}(t) = \sum_{i=1}^{N} h_{i,j}\left(t + \Delta T_{q,i}\right) \tag{27}$$

After the conversion the data sets are processed into an image with the different PWI techniques. For PWNA and PWAPP the images are formed using plane waves transmitted at 64 equally spaced angles -12.6° : 0.4° : 12.6° inside the couplant. The angles are specified to produce coverage close to -60° to +60° inside a flat front surface specimen of the same material. During the processing with PWNA the central ray refracted angles for each pipe radius are recorded. Those are input into PWAT, which requires input angles in the specimen rather than the couplant. Furthermore, in all PWI the exact geometry and location of the simulated front surface is used, thereby ignoring the effects of surface reconstruction accuracy. These steps ensure the techniques' comparison is done under as similar as possible conditions.

Firstly, a point reflector 10 mm away from the phased array centreline and at 10 mm depth beneath the front surface is imaged. The array and scatterer configuration to scale is shown in Figure 2a. This point-reflector is selected since it is just outside of the aperture and at a depth often specified as the nominal thickness of pipelines in the oil and gas industry. Hence it can be regarded as a representative of the response from a small defect on the outer surface of a pipe. Figure 3 displays results with the 3 PWI techniques for front surface radii of 50, 100 and 300 mm. All images are 7×7 mm, centered onto the scatterer, and plotted on a -40 to 0 dB scale relative to the peak amplitude. The images show a clear central indication of the point reflector and can be used to qualitatively compare the algorithms. A performance improvement of the adapted techniques over PWNA is easily observable at front surface radii of 50 and 100 mm, while at larger front surface radii the performance of the 3 PWI techniques is similar.

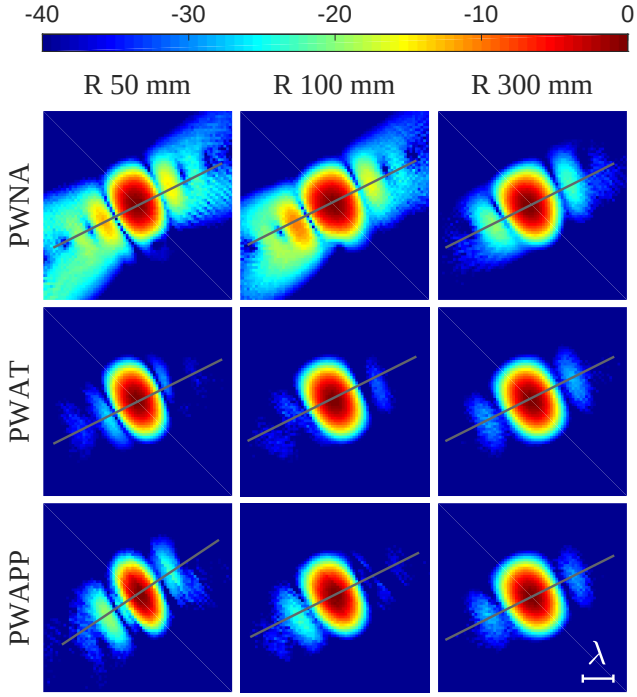

Fig. 3: Point spread function plot of a defect 10 mm away from the centre of the phased array in the lateral direction and 10 mm under a front surface of different radii (Colour intensity in dB). The grey lines indicate the positions of the intensities plotted in Fig. 4.

To compare the point-spread functions of the algorithms for the different front surface radii quantitatively, the cross section of the reflector indications are examined. Those are detected automatically by fitting a bounding box around pixels above a -20 dB threshold. A line is plotted through the maximum intensity observed in an image. This line is parallel to the side of the bounding box that is closest to being perpendicular to the direction of the central ray (i.e. the transverse cross section through the reflector indication). The lines are shown in Figure 3. The intensities along those lines are recorded and summarised for the 3 different front surface radii in Figure 4. PWNA exhibits a wider main lobe than PWAT and PWAPP. The main lobe widths for R 50 mm curvature are: PWNA 1.12 mm; PWAT 0.98 mm; and PWAPP 0.79 mm. This is a reduction of 12.5% and 29.5% with respectively PWAT and PWAPP. The results for the 3 methods from the larger curvature R 300 mm surface are much closer. The main lobe widths are: PWNA 1.14 mm; PWAT 1.09 mm; and PWAPP 1.10 mm. PWNA also yields higher intensity side-lobes, reaching -12.5 dB and -10.5 dB respectively for the front

This article has been accepted for publication in a future issue of this journal, but has not been fully edited. Content may change prior to final publication. Citation information: DOI 10.1109/TUFFC.2020.2969083, IEEE Transactions on Ultrasonics, Ferroelectrics, and Frequency Control

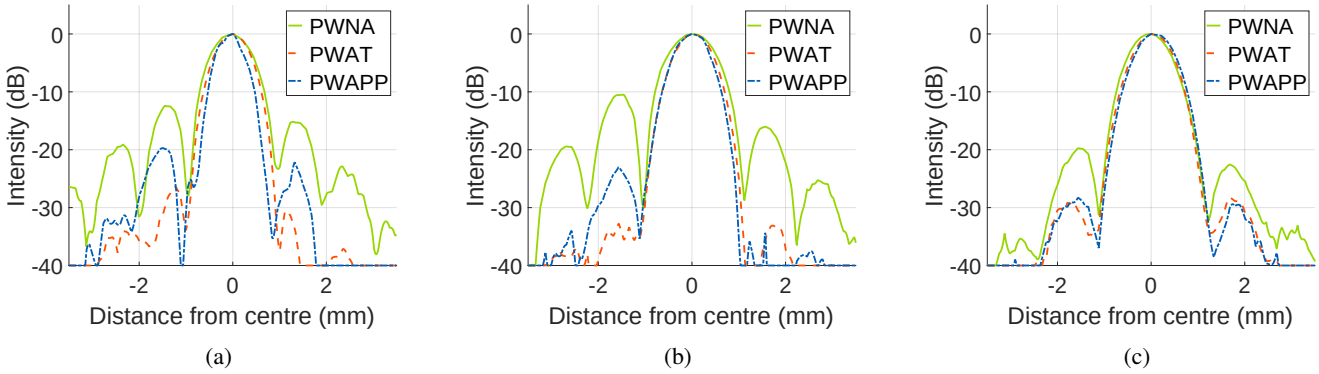

Fig. 4: Point spread function plot of a defect 10 mm away from the centreline of the phased array and 10 mm under a front surface of radii: (a) R 50 mm; (b) R 100 mm; (c) R 300 mm.

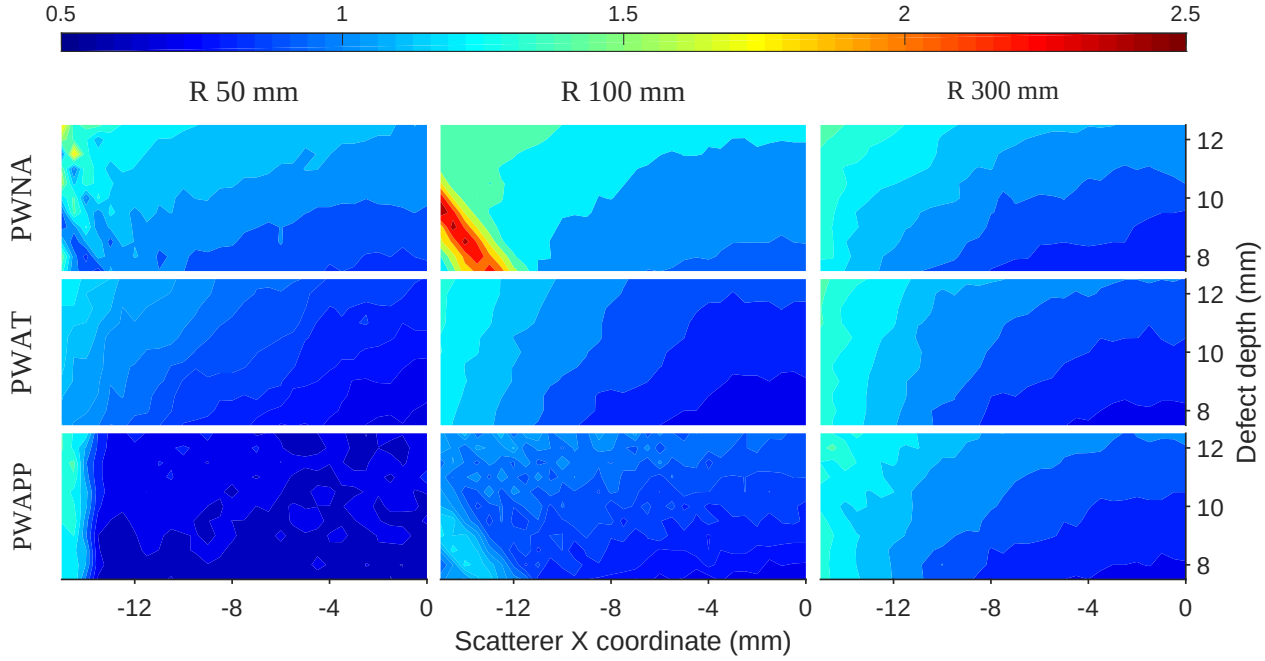

Fig. 5: $API_{\text{-6 dB}}$ (shown as colour intensity) produced by PWNA, PWAT and PWAPP for the scatterers from Fig. 2b under a front surface of radius between 50 and 300 mm.

surfaces of R 50 mm and R 100 mm. For a R 50 mm front surface, the highest intensity side-lobe produced by PWAT is -26.4 dB, while PWAPP highest output is -19.7 dB. When focusing through a R 300 mm surface, PWNA, PWAT, and PWAPP produce side lobes of maximum intensity respectively -19.7, -28.2 and -28.3 dB.

To summarise the results from all PWI techniques for all front surface radii, the array performance index (API) [6] was used. API is defined as the area S of the ultrasonic array image above a certain threshold normalised by the wavelength squared. For a -6 dB threshold this is as follows:

$$API_{\text{-6 dB}} = \frac{S_{\text{-6 dB}}}{\lambda^2} \tag{28}$$

The PWNA, PWAT and PWAPP $API_{\text{-6 dB}}$ results are summarised in Figure 5. Those have been plotted onto the same 0.5 to 2.5 intensity colour scale to ensure comparisons can be drawn between the different figures. Lower $API_{\text{-6 dB}}$ implies smaller focal spot, hence the better results tend towards blue in the colour plots.

All plots in Figure 5 show significantly better performance for scatterers simulated under the phased array aperture (-9.5 mm to 0 mm X coordinate) than for those outside of it. This is due to the specified firing pattern producing better coverage of the area (i.e. higher number of transmitted plane waves actually insonify the reflectors). Comparing between the different algorithms, the expected convergence towards similar results is observed with increasing front surface radius. At R 300 mm, the PWNA and PWAT $API_{\text{-6 dB}}$ results are already stable, with the latter slightly outperforming the first in imaging the deeper reflectors. PWAPP is generally comparable to PWAT, but exhibits some oscillations for reflectors outside

This article has been accepted for publication in a future issue of this journal, but has not been fully edited. Content may change prior to final publication. Citation information: DOI 10.1109/TUFFC.2020.2969083, IEEE Transactions on Ultrasonics, Ferroelectrics, and Frequency Control

of the phased array aperture. These inconsistencies in the PWAPP results can be explained through observing Fig. 1d again. As stated, for some transmission angles one part of the plane wave will refract on top of another resulting in the insonification of a region multiple times by the same plane wave. Since the plane wave is split into a finite number of sections during imaging, abrupt rather than continuous and smooth change in intensity can be observed between adjacent reflectors if they are located in different sections.

Across all 3 PWI techniques the results for the smaller front surface radii (particularly R 50 mm) give generally lower API values, suggesting superior imaging performance. However, this is somewhat misleading. If Figures 3 and 4 are re-examined, the width and area of the main lobe indications for smaller radii front surfaces are definitely smaller. Nevertheless, this does not necessarily signify better results, as the images are polluted by artifacts from the side lobes. While the $API_{\text{-6 dB}}$ generally catches only the main lobe indications, occasionally it will include some of the artifacts produced by the side-lobes. For example, this is the cause of the irregularly high $API_{\text{-6 dB}}$ pattern in the PWNA at curvature radius of 100 mm contour (Figure 5). Disregarding the small regions in which the performance is dominated by such factors, all techniques are capable of imaging the defect in its correct location at an intensity (above -6 dB) sufficiently high for detection purposes. The performance is better for shallower defects under the phased array aperture and the adapted techniques both outperform PWNA in inspections through smaller radius surfaces.

V. Experimental Examples

A. PWI of a half-pipe specimen

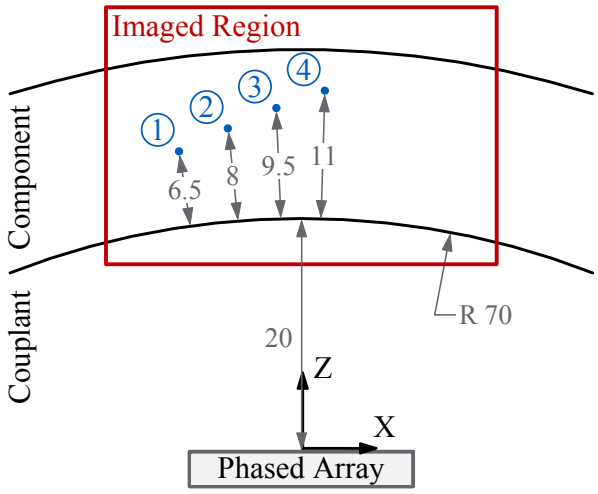

Fig. 6: Inspection configuration of half-pipe specimen with side-drilled holes (dimensions in mm).

Experimental FMC data have been collected from a carbon steel half-pipe specimen. A dimensioned drawing of the sample is shown in Figure 6. The inspection configuration is in immersion with the array positioned so that its centre is 20 mm away from the portion of pipe surface directly under it. The inspection parameters are given in Table I, except the FMC has been captured with with a phased array of 128 instead of 64 elements. The defects contained in the specimen are side-drilled holes of diameter 1.5 mm. Those are numbered 1 to 4 in Figure 6. Images of the holes, formed with the 3 PWI techniques, are compared. A reference TFM image is also provided. The first comparison, similarly to the one in the previous section, ignores the effects of the front surface reconstruction accuracy. The second one demonstrates the advantageous ability of PWAPP to extract a surface profile and form high sensitivity images from the same data without any transmission adjustments.

To begin with, the pipe front surface is imaged with TFM using the full 128 elements aperture. Nodes are assigned to it according to the highest intensities observed in each depth line of the image. A circle is fitted to the nodes using a MATLAB Files Exchange code [40]. This reconstructed surface is input into all imaging algorithms. The FMC conversion into plane wave data follows equations 12, 26 and 27. The imaging inside the pipe specimen is in direct mode with longitudinal waves using only the central 64 array elements. The performance of the 3 PWI techniques with synthesized 64 plane wave transmissions at angles -12.6° : 0.4° : 12.6° is compared to that of TFM. The results are presented in Figure 7. The images have been normalised with respect to a root mean square (RMS) intensity value calculated in a region with no features, shown as a grey dashed-sides rectangle. The final intensity is plotted onto a 0 to 40 dB scale above this RMS noise value.

Side-drilled holes 2 to 4 are clearly visible in all images. The indication from defect 1 is noticeably fainter even when using the more advanced imaging algorithms and is at the intensity level of the imaging artifacts in the PWNA image. The Signal-to-Noise Ratios (SNR) are recorded for the defects through extracting the highest observed intensity from an indicator in the images formed with each algorithm. Those are summarised in Figure 8a. TFM is the best performing technique followed by PWAT. With an optimal choice of plane wave firing angles, the information contained in the FMC and the plane wave data subsequently used to form the images should be the same [33]. However, no firing angles optimisation study is attempted, causing the marginally worse SNR in PWAT. PWAT's superiority to other PWI is expected, given the adaptation in the beam forming to produce a specific plane wave and ensure the inspected region is covered uniformly. However, in practice this would require either precise measurements of the orientation of the phased array w.r.t. the component surface or multiple transmission cycles initially intended at surface reconstruction and later at component internal imaging. In contrast, the PWAPP algorithm does not require any adjustments to the transmission pattern and yields performance close to the TFM (5 to 13% lower SNR). As expected in such a small radius curvature PWNA results are inadequate. The performance drop is evident, when imaging through a portion of the surface, whose normal is forming a larger angle with the phased array normal (defects 1 and 2).

The main advantage of PWI over other ultrasonic imaging techniques is in the ability to produce high sensitivity images

This article has been accepted for publication in a future issue of this journal, but has not been fully edited. Content may change prior to final publication. Citation information: DOI 10.1109/TUFFC.2020.2969083, IEEE Transactions on Ultrasonics, Ferroelectrics, and Frequency Control

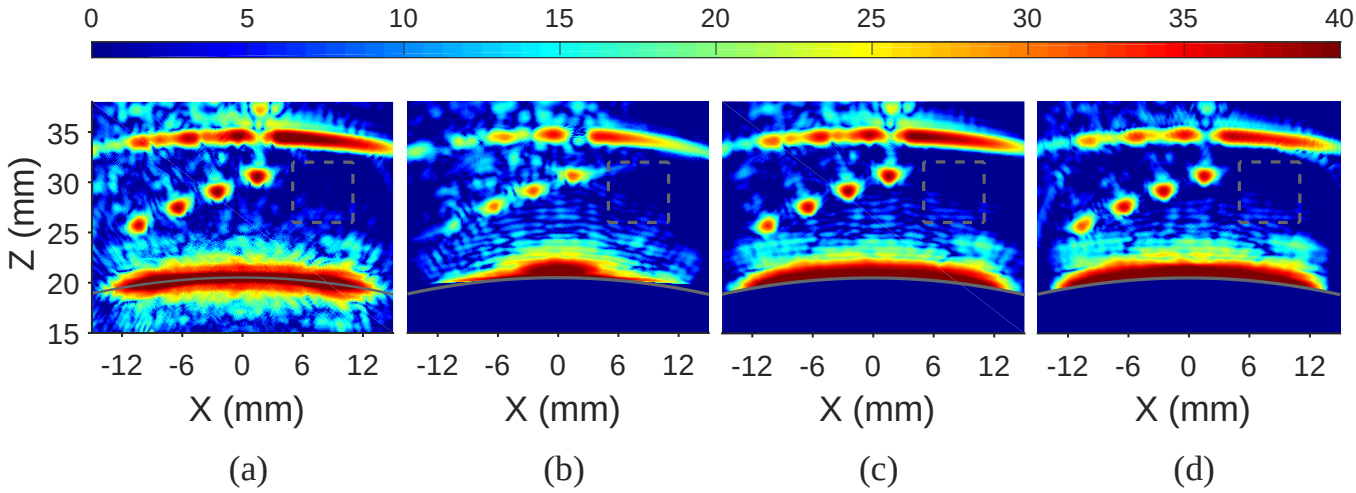

Fig. 7: Imaging of side-drilled holes in half-pipe specimen (Surface reconstructed from FMC data, colour intensities in dB, RMS noise region for normalisation in grey rectangle): (a) TFM; (b) PWNA (64 firings); (c) PWAT (64 firings); and (d) PWAPP (64 firings).

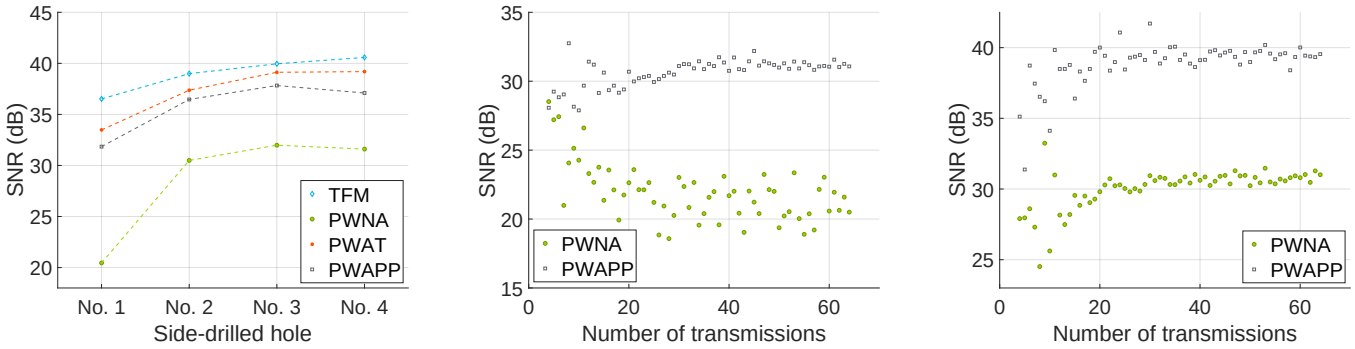

Fig. 8: Side-drilled holes SNRs: (a) w.r.t imaging algorithm, summary of Fig 7; (b) Side-drilled hole 1 w.r.t. number of plane wave transmissions; (c) Side-drilled hole 4 SNR w.r.t. number of plane wave transmissions.

with few transmissions. PWAT requires knowledge of the front surface prior to these transmissions, in order to adapt the wave fronts. This information could be obtained (e.g. ultrasonically), but at the expense of additional measurements and acquisition time. Conversely, PWNA and PWAPP both involve the transmission of plane waves into the couplant and therefore do not require prior knowledge of the front surface; instead the front surface is recovered from the data prior to image form. To demonstrate this and particularly the improvements PWAPP boasts over PWNA with the same number of transmissions, the same setup from Fig. 6 and captured FMC data are considered. However, the plane wave data are synthesised before the surface nodes extraction, which is now done from a PWI rather than a TFM image. Therefore, the same data are used for both the extraction and subsequent imaging inside the component. Additionally, the front surface is directly defined as the points resulting from applying a moving average filter on the extracted nodes instead of a forced circular fit. Figure 9 shows the PWNA and PWAPP results with 4 and 16 plane wave firings equally spaced in terms of angles between -12.6° and 12.6° in the couplant. The PWNA 4 transmissions result (Fig. 9a) shows detection of all defects, albeit at SNR of 29.2 dB or lower. Parts of the back surface, mostly behind the holes, cannot be imaged. The PWAPP 4 firings image (Fig. 9b) shows the distortion of the plane waves upon refraction into the specimen and explains the portions of the back surface indication are missing because they have not been insonified. In place of defect 1 multiple indications are observed and detection is difficult. Side-drilled hole 2 is imaged at SNR equivalent to the one produced by PWNA. Defects 3 and 4 are below the phased array aperture and display much higher SNR of respectively 38.7 and 35.1 dB. Increasing the number of transmissions to 16 in PWNA (Fig. 9c) displays more of the back surface but does not offer a significant increase in SNR of holes. The maximum SNR gain is 2.9 dB for defect 2, while defects 1 and 3 even exhibit a drop. PWAPP with 16 transmissions (Fig. 9d) results in a large 12.8 dB increase of SNR for defect 2, but little to no improvement for the rest of the side-drilled holes.

Figures 8b and 8c show the SNR of defects 1 and 4 with

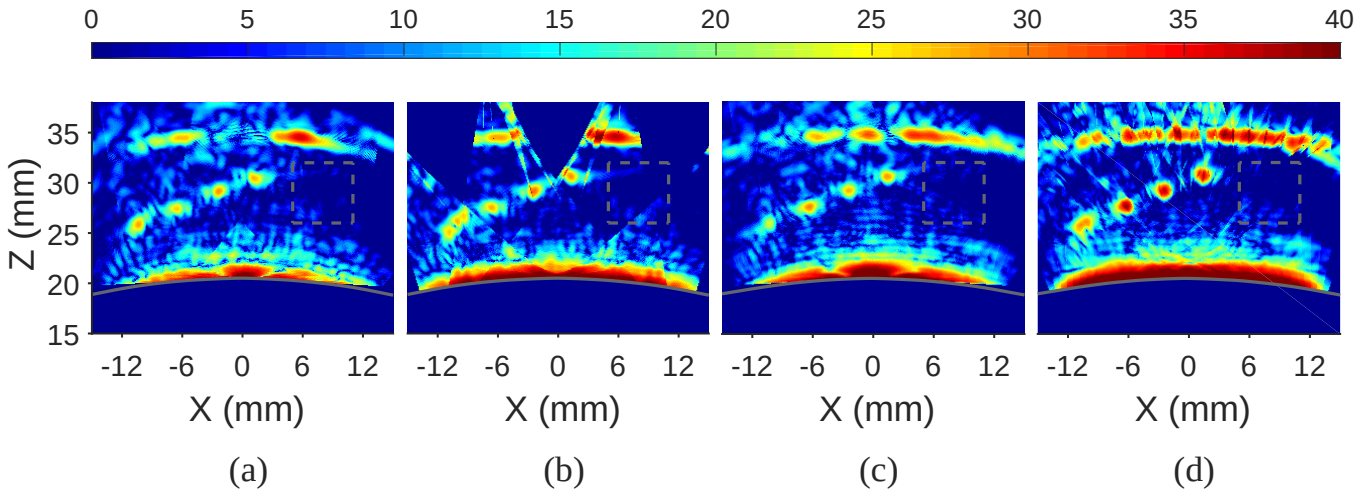

Fig. 9: Imaging of side-drilled holes in half-pipe specimen (Surface reconstructed directly from plane wave data, colour intensities in dB, RMS noise region for normalisation in grey rectangle): (a) PWNA (4 firings); (b) PWAPP (4 firings); (c) PWNA (16 firings); and (d) PWAPP (16 firings).

respect to number of transmissions for PWNA and PWAPP. The transmit plane wave angles are equally spaced between -12.6° and 12.6° in the couplant. Initially, increasing the number of transmissions results in an increase of SNR, except for defect 1 imaged with PWNA. Defect 1 is not under the array aperture. Hence, it is insonified only by oblique front surface incidence plane waves, which are severely distorted upon the refraction. This leads to unpredictability and instability in the PWNA side-drilled hole 1 results, further manifested as the larger dispersion of SNR values even for higher number of transmissions. The rest of the results in Fig. 8 display a nearly linear increase in SNR from 4 to 32 transmissions. From 32 to 64 transmissions saturation is reached and there is no apparent gain in SNR. This proves the statement to the ability of PWI to produce high sensitivity images even through unknown surfaces with fewer transmission than TFM. Finally, regardless of the number of firings, PWAPP displays SNR of approximately 10 and 8 dB higher than PWNA respectively for defects 1 and 4. The data capture required by the 2 PWI algorithms is the same, which shows PWAPP is the superior post-processing technique.

B. PWAPP through a sinusoidal surface

To test the limitations of PWAPP, focusing through a sinusoidal surface is examined. A dimensioned diagram of the experimental configuration is shown in Figure 10a. The surface is defined with a sine wave of 2 mm amplitude and 40 mm period. The defects contained in the specimen are 5 side-drilled holes of diameter 1 mm, numbered 1 through 5 in Fig. 10a. The configuration is in immersion with the phased array positioned so that it is approximately 20 mm away from the mean of the component surface, and its center is under the central hole. The parameters used are given in Table I, except again the FMC is collected using all 128 elements. Additionally, the temperature of the water is measured to accurately estimate its speed of sound (1467.3 m/s).

Firstly, the surface is reconstructed from a TFM image through applying a moving average filter to the extracted surface nodes. The procedure is described in Section V-A. This profile is subsequently input in the imaging algorithms to simulate focusing through a known specimen surface and position. The imaging is in direct mode with longitudinal waves using only the central 64 elements. The same RMS normalisation approach is used as for the half-pipe specimen results, but the intensity plots are on a 12 to 52 dB scale. The distortion exerted onto a single plane wave transmitted at 5° is examined. This is shown schematically in Figure 10b. The sections of the plane wave transmitted from the elements at the ends of the phased array do not refract into the specimen, resulting in a smaller effective firing aperture. Additionally, upon refraction the ray angles result in a focused at about 10 mm under the component surface pattern, which then diverges with depth in the sample. However, even after this complex interaction of the plane wave with the component surface, the data collected can be used to interpret the condition of the specimen. The PWAPP image formed from this single plane wave is shown in Figure 10c. All defects are visible albeit polluted with some artifacts. If a large number of plane waves (64 at angles: -12.6° : 0.4° : 12.6°) are transmitted the quality produced is close to that of TFM. The results presented in Figures 11a and 11b serve as a comparison between TFM and PWAPP. The central 3 holes are represented equally well in both images. TFM outputs a higher intensity for the outer two holes suggesting higher angular coverage. The shallowest hole in the PWAPP image is also split into a double indication which could potentially be misleading.

Due to the extreme surface normal angles, entire plane waves from the transducer can hardly refract into the specimen (and vice versa). Therefore, using PWNA or PWAT significantly reduces the range of possible plane wave transmission angles. However, PWAPP is not restricted in this manner because it processes the plane waves in portions, rather than in

This article has been accepted for publication in a future issue of this journal, but has not been fully edited. Content may change prior to final publication. Citation information: DOI 10.1109/TUFFC.2020.2969083, IEEE Transactions on Ultrasonics, Ferroelectrics, and Frequency Control

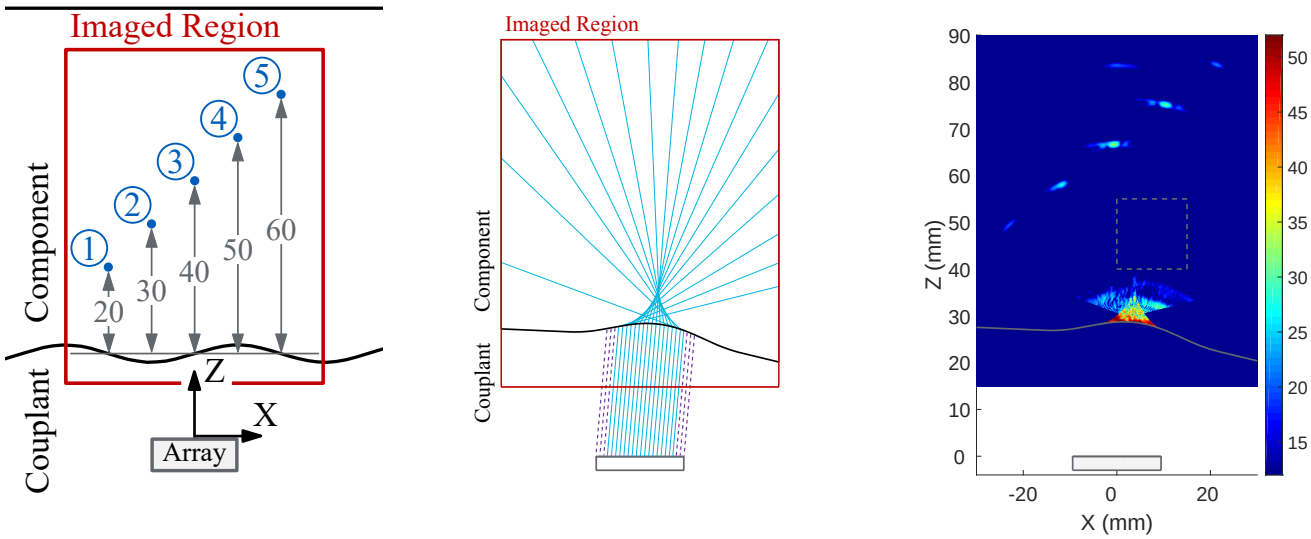

(a) (b) (c)

Fig. 10: (a) Inspection configuration of sinusoidal front surface specimen (dimensions in mm); (b) Distortion profile of a plane wave fired at 5° upon refraction through a sine wave front surface specimen; (c) PWAPP image formed with the 5° plane wave (Colour intensities in dB, RMS noise region for normalisation in grey rectangle).

their entirety. It tracks which sections are transmitted into the specimen and images only with them. As shown in Fig. 10c, even partially refracted plane waves can contain valuable information about a component. This ability to utilise all available data makes PWAPP particularly valuable in inspections through unknown complex surfaces in immersion. Figures 11c and 11d demonstrate the performance of PWAPP with limited number of transmissions. The plane wave angles are again equally spaced between -12.6° and 12.6° in the couplant. The same setup and collected FMC is used, however the surface is reconstructed directly from a PWI image formed after the plane wave data is synthesised. This surface reconstruction appears less representative than the one from a TFM image in the regions that are not directly above the array aperture (comparison of the dark grey lines at depths between 20 and 30 mm in Figures 11b and 11d). The 4 transmissions PWAPP image (Fig. 11c) shows high SNR for defect 3 (37.5 dB), but otherwise outputs multiple artifacts around the real indications. It is considered insufficient for the detection of all defects. PWAPP with 16 transmissions (Fig. 11d) increases the SNR for holes 2, 3 and 4 to respectively significantly (respectively 38.9, 40.3, and 39 dB) and these are clearly detectableDefect 1 shows a double indication. Both it and defect 5 display significantly lower intensity than the holes directly above the phased array aperture. Figure 12 investigates the PWAPP SNR performance w.r.t. number of transmissions for holes 1, 3, and 5. As for the half-pipe specimen, near linear increase in SNR is observed at lower number of transmissions (up to 32) after which a saturation is reached and no apparent improvement is gained by acquiring more data. The SNR saturation value for defect 3 is approximately 44 dB, which is significantly higher than the 34 and 31 dB respectively for holes 1 and 5. This discrepancy results from the poor coverage in regions away from the array aperture even at relatively shallow depths.

VI. Conclusions

A new PWI approach is proposed using adaptation in post-processing rather than in transmission. This implementation is shown to produce images of comparable quality to ones using delay adaptations in transmission, while being potentially more robust when there is misalignment in the array orientation or the component surface is unknown. The algorithm's ability to image a perfect reflector through different radius concave curvature is investigated through simulation. It is established that there is natural focusing present when imaging through smaller radii surfaces resulting in smaller point spread function and apparent better performance. The PWAPP imaging is also tested experimentally onto a carbon steel sample containing side-drilled holes. All defects are identifiable and their SNR is comparable to the ones produced by PWAT and TFM. Finally, the technique was tested in imaging of side-drilled holes under a sinusoidal surface. The complex surface restricts the range of angles for which a plane wave can refract into the component in its entire width. PWAPP is readily applicable in this scenario, since it utilises the available data from even partially transmitted plane waves. With a number of transmissions equal to the number of array elements, it yields images similar to TFM, while even with a quarter of the firings it detects all the defects.

Acknowledgment

The authors would like to thank Baker Hughes and the UK Engineering and Physical Sciences Research Council for sponsoring this project. The authors are grateful to S. Iles for manufacturing the test components.

This article has been accepted for publication in a future issue of this journal, but has not been fully edited. Content may change prior to final publication. Citation information: DOI 10.1109/TUFFC.2020.2969083, IEEE Transactions on Ultrasonics, Ferroelectrics, and Frequency Control

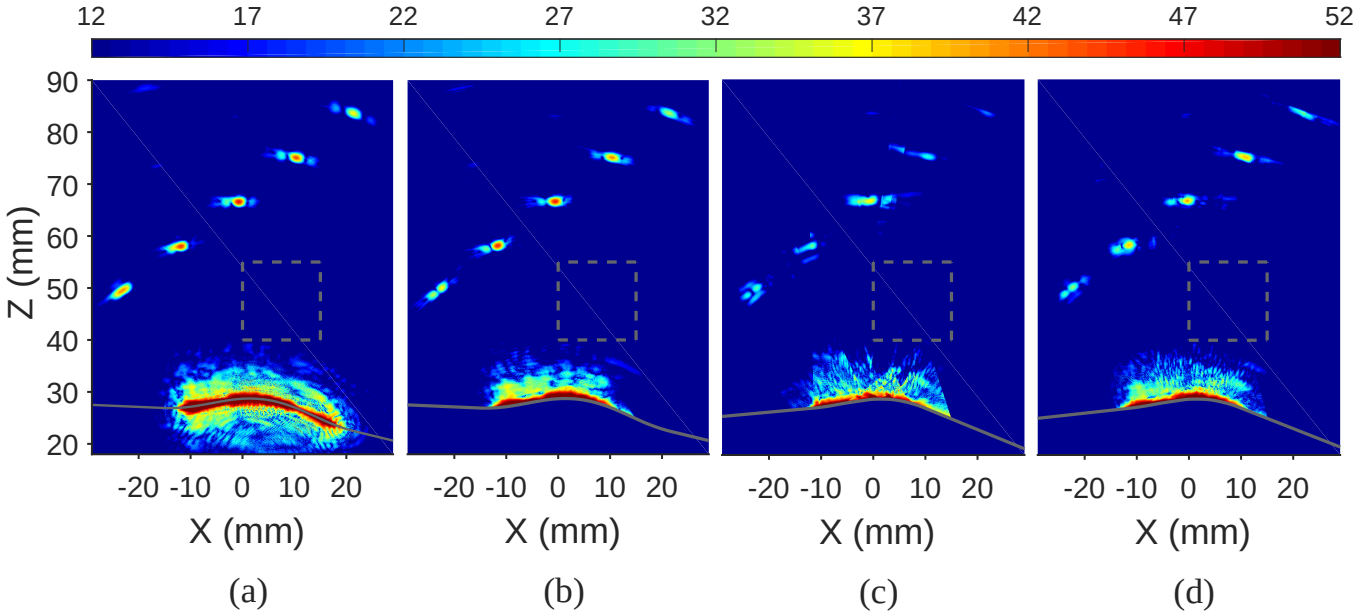

Fig. 11: Sine wave front surface component imaging (Colour intensities in dB, RMS noise region for normalisation in grey rectangle): (a) TFM; (b) PWAPP (64 firings, surface reconstructed from FMC data); (c) PWAPP (4 firings, surface reconstructed directly from plane wave data); (d) PWAPP (16 firings, surface reconstructed directly from plane wave data).

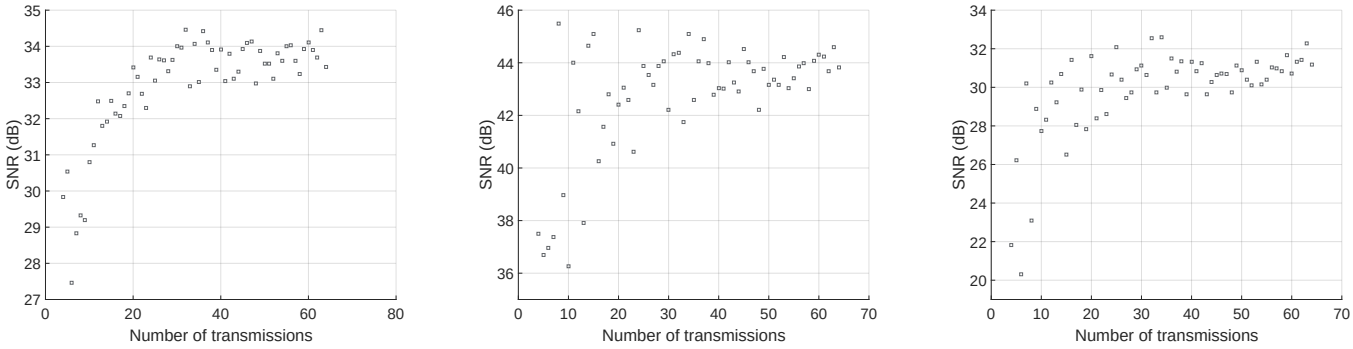

Fig. 12: Point spread function plot of a defect 10 mm away from the centreline of the phased array and 10 mm under a front surface of radii: (a) defect 1; (b) defect 3; (c) defect 5.

REFERENCES

[1] M. Papaelias, C. Roberts, and C. L. Davis, "A review on non-destructive evaluation of rails: state-of-the-art and future development," *Proc. Inst. Mech. Eng. Pt. F J. Rail Rapid Transit*, vol. 222, no. 4, pp. 367–384, 2008.

[2] I. Komura, T. Hirasawa, S. Nagai, J. Takabayashi, and K. Naruse, "Crack detection and sizing technique by ultrasonic and electromagnetic methods," *Nucl. Eng. Des.*, vol. 206, pp. 351–362, 2001.

[3] D. Allen, P. Senf, I. Lachtchouk, and S. Falter, "Update on Ultrasonic Phased Array Crack Detection," *Pipeline & Gas Journal*, pp. 44–50, 2010.

[4] P. D. Wilcox, "Ultrasonic arrays in NDE: Beyond the B-scan," *Proc. Ann. Rev. Prog. QNDE*, vol. 1511, no. 1, pp. 33–50, 2013.

[5] Ö. Oralkan, A. S. Ergun, J. A. Johnson, M. Karaman, U. Demirci, K. Kaviani, T. H. Lee, and B. T. Khuri-Yakub, "Capacitive micromachined ultrasonic transducers: Next-generation arrays for acoustic imaging?," *IEEE Trans. Ultrason., Ferroelectr., Freq. Control*, vol. 49, no. 11, pp. 1596–1610, 2002.

[6] C. Holmes, B. W. Drinkwater, and P. D. Wilcox, "Post-processing of the full matrix of ultrasonic transmitreceive array data for non-destructive evaluation," *NDT and E Int.*, vol. 38, pp. 701–711, 2005.

[7] A. J. Hunter, B. W. Drinkwater, and P. D. Wilcox, "Autofocusing ultrasonic imagery for non-destructive testing and evaluation of specimens with complicated geometries," *NDT and E Int.*, vol. 43, no. 2, pp. 78–85, 2010.

[8] S. Chatillon, G. Cattiaux, M. Serre, and O. Roy, "Ultrasonic non-destructive testing of pieces of complex geometry with a flexible phased array transducer," *Ultrasonics*, vol. 38, no. 1, pp. 131–134, 2000.

[9] K. Shi, K. Que, and D. Guo, "Flexible Ultrasonic Phased-Array Probe," *Tsinghua Sci. Technol.*, vol. 9, no. 5, pp. 574–577, 2004.

[10] O. Casula, C. Poidevin, G. Cattiaux, and P. Dumas, "Control of complex components with smart flexible phased arrays," *AIP Conf.*, vol. 820 I, pp. 829–836, 2006.

[11] C. J. L. Lane, "The inspection of curved components using flexible ultrasonic arrays and shape sensing fibres," *Case Stud. Nondestr. Test. Eval.*, vol. 1, pp. 13–18, 2014.

[12] M. Sutcliffe, M. Weston, P. Charlton, K. Donne, B. Wright, and I. Cooper, "Full matrix capture with time-efficient auto-focusing of unknown geometry through dual-layered media," *Insight*, vol. 55, no. 6, pp. 297–301, 2013.

[13] R. Long and P. Cawley, "Further development of a conformable phased array device for inspection over irregular surfaces," *AIP Conf.*, vol. 975, no. 2008, pp. 754–761, 2008.

[14] S. Mahaut, O. Roy, C. Beroni, and B. Rotter, "Development of phased array techniques to improve characterization of defect located in a component of complex geometry," *Ultrasonics*, vol. 40, no. 1-8, pp. 165–169, 2002.

[15] P. Calmon, E. Iakovleva, A. Fidahoussen, G. Ribay, and S. Chatillon, "Model based reconstruction of UT array data," *AIP Conf.*, vol. 975, no. March 2008, pp. 699–706, 2008.

[16] A. Fidahoussen, P. Calmon, M. Lambert, S. Paillard, and S. Chatillon, "Imaging of defects in several complex configurations by simulation-helped processing of ultrasonic array data," *AIP Conf.*, vol. 1211, no. 2010, pp. 847–854, 2010.

[17] J. Zhang, B. W. Drinkwater, and P. D. Wilcox, "Efficient immersion imaging of components with nonplanar surfaces," *IEEE Trans. Ultrason., Ferroelectr., Freq. Control*, vol. 61, no. 8, pp. 1284–1295, 2014.

[18] R. E. Malkin, A. C. Franklin, R. L. Bevan, H. Kikura, and B. W. Drinkwater, "Surface reconstruction accuracy using ultrasonic arrays: Application to non-destructive testing," *NDT and E Int.*, vol. 96, no. November 2017, pp. 26–34, 2018.

[19] S. Kidera, T. Sakamoto, and T. Sato, "A robust and fast imaging algorithm with an envelope of circles for UWB pulse radars," *IEICE Trans. Commun.*, vol. E90-B, no. 7, pp. 1801–1809, 2007.

[20] W. Kerr, S. G. Pierce, and P. Rowe, "Investigation of synthetic aperture methods in ultrasound surface imaging using elementary surface types," *Ultrasonics*, vol. 72, pp. 165–176, 2016.

[21] J. Zhang, B. W. Drinkwater, P. D. Wilcox, and A. J. Hunter, "Defect detection using ultrasonic arrays: The multi-mode total focusing method," *NDT and E Int.*, vol. 43, no. 2, pp. 123–133, 2010.

[22] N. Budyn, R. Bevan, J. Zhang, A. J. Croxford, and P. D. Wilcox, "A Model for Multiview Ultrasonic Array Inspection of Small Two-Dimensional Defects," *IEEE Trans. Ultrason., Ferroelectr., Freq. Control*, vol. 66, no. 6, pp. 1129–1139, 2019.

[23] R. Bevan, J. Zhang, N. Budyn, A. J. Croxford, and P. D. Wilcox, "Experimental Quantification of Noise in Linear Ultrasonic Imaging," *IEEE Trans. Ultrason., Ferroelectr., Freq. Control*, vol. 66, no. 1, pp. 79–90, 2019.

[24] M. V. Felice, A. Velichko, and P. D. Wilcox, "Accurate depth measurement of small surface-breaking cracks using an ultrasonic array post-processing technique," *NDT and E Int.*, vol. 68, pp. 105–112, 2014.

[25] R. K. Rachev, P. D. Wilcox, A. Velichko, K. McAughey, and J. Giese, "Ultrasonic immersion testing for crack detection and depth sizing in large diameter pipes," in *ECNDT Proc.*, pp. 1–8, 2018.

[26] M. Karaman, P. C. Li, and M. O 'donnell, "Synthetic Aperture Imaging for Small Scale Systems," *IEEE Trans. Ultrason., Ferroelectr., Freq. Control*, vol. 42, no. 3, pp. 429–442, 1995.

[27] G. R. Lockwood, P. C. Li, M. O'Donnell, and F. Stuart Foster, "Optimizing the radiation pattern of sparse periodic linear arrays," *IEEE Trans. Ultrason., Ferroelectr., Freq. Control*, vol. 43, no. 1, pp. 7–14, 1996.

[28] L. Moreau, B. W. Drinkwater, and P. D. Wilcox, "Ultrasonic imaging algorithms with limited transmission cycles for rapid nondestructive evaluation," *IEEE Trans. Ultrason., Ferroelectr., Freq. Control*, vol. 56, no. 9, pp. 1932–1944, 2009.

[29] S. Bannouf, S. Robert, O. Casula, and C. Prada, "Data set reduction for ultrasonic TFM imaging using the effective aperture approach and virtual sources," in *J. Phys: Conf. Ser.*, 2013.

[30] G. Montaldo, M. Tanter, J. Bercoff, N. Benech, and M. Fink, "Coherent plane-wave compounding for very high frame rate ultrasonography and transient elastography," *IEEE Trans. Ultrason., Ferroelectr., Freq. Control*, vol. 56, no. 3, pp. 489–506, 2009.

[31] A. Austeng, C. C. Nilsen, A. C. Jensen, S. P. Nasholm, and S. Holm, "Coherent plane-wave compounding and minimum variance beamforming," in *Proc. IEEE Int. Ultrason. Symp.*, pp. 2448–2451, IEEE, oct 2011.

[32] L. Le Jeune, S. Robert, E. Lopez Villaverde, and C. Prada, "Plane Wave Imaging for ultrasonic non-destructive testing: Generalization to multimodal imaging," *Ultrasonics*, vol. 64, pp. 128–138, 2016.

[33] A. Velichko and A. J. Croxford, "Strategies for data acquisition using ultrasonic phased arrays," *Proc. Royal Soc. A*, vol. 474, 2018.

[34] L. Le Jeune, S. Robert, and C. Prada, "Plane wave imaging for ultrasonic inspection of irregular structures with high frame rates," *AIP Conf.*, vol. 1706, pp. 020010–1:6, 2016.

[35] S. Robert, O. Casula, O. Roy, and G. Neau, "Real-time nondestructive testing of composite aeronautical structures with a self-adaptive ultrasonic technique," *Meas. Sci. Technol.*, vol. 24, no. 7, pp. 207–212, 2013.

[36] N. Q. Nguyen and R. W. Prager, "High-resolution ultrasound imaging with unified pixel-based beamforming," *IEEE Trans. Med. Imag.*, vol. 35, no. 1, pp. 98–108, 2016.

[37] A. S. Glassner, *An Introduction to Ray Tracing*. Academic Press Limited, 2nd ed., 1990.

[38] L. W. Schmerr, *Fundamentals of Ultrasonic Nondestructive Evaluation - A Modeling Approach*. Springer International Publishing, 2 ed., 2016.

[39] J. Krautkramer and H. Krautkramer, *Ultrasonic Testing of Materials*. Verlag Berlin Heidelberg: Springer, 4 ed., 1990.

[40] N. Chernov, "MATLAB File Exchange: Circle Fit (Pratt method)," 2009.

Rosen K. Rachev was born in Burgas, Bulgaria, in 1993. He received the M.Eng. degree in Mechanical Engineering from the University of Bristol, Bristol, U.K., in 2016. He is currently pursuing the D.Eng. degree in Nondestructive Evaluation in the Ultrasonics and Nondestructive Testing Research Group, University of Bristol. He is working on advanced ultrasonic data processing algorithms for pipeline in-line inspections, and his project is sponsored by Baker Hughes. His research interests include non-destructive evaluation for the oil and gas industry, ultrasonic phased array surface reconstruction, adaptive imaging, and defect characterisation.

Paul D. Wilcox was born in Nottingham, U.K., in 1971. He received the M.Eng. degree in engineering science from the University of Oxford, Oxford, U.K., in 1994, and the Ph.D. degree from Imperial College London, London, U.K., in 1998.

He remained in the Non-Destructive Testing (NDT) Research Group at Imperial College London as a Research Associate until 2002, working on the development of guided-wave array transducers for large-area inspection. Since 2002, he has been with the Department of Mechanical Engineering at the University of Bristol, Bristol, U.K., where his current title is Professor of dynamics. He held an EPSRC Advanced Research Fellowship in Quantitative Structural Health Monitoring from 2007 to 2012, was the Head of the Mechanical Engineering Department from 2015 to 2018, and has been a fellow of the Alan Turing Institute for Data Science, London, U.K., since 2018. In 2015, he was a Co-Founder of Inductosense Ltd., Bristol, a spin-out company that is commercializing inductively coupled embedded ultrasonic sensors. His research interests include array transducers, embedded sensors, ultrasonic particle manipulation, long-range guided-wave inspection, structural health monitoring, elastodynamic scattering, and signal processing.

Alexander Velichko was born in Krasnodar, Russia, in 1975. He received the M.Sc. degree in applied mathematics from the Kuban State University, Krasnodar, Russia, in 1998, and the Ph.D. degree from the Rostov State University, Rostov-on-Don, Russia, in 2002, with a focus on the investigation of wave fields caused by internal vibration sources in layered elastic medium. From 2005 to 2012, he was a Research Associate with the Ultrasonics and Nondestructive Testing Research Group, University of Bristol, Bristol, U.K. In 2012, he was appointed Lecturer with the Department of Mechanical Engineering, University of Bristol. His current research interests include the mathematical modeling of propagation and the scattering of elastic waves, ultrasonic imaging using arrays, and guided waves and signal processing.

Kevin L. McAughey received the B.Sc. degree in physics from The University of Warwick, Coventry, U.K., in 2009, the M.Sc. degree by Research in high temperature piezoelectric films in 2011, and the Ph.D. degree in non-destructive evaluation in 2015, focusing on guided wave ultrasonics generated and detected by electromagnetic acoustic transducers. He joined Baker Hughes in 2014, where he continued to work EMATs and guided waves, while also gaining experience in other disciplines, including phased array ultrasonics and magnetic flux leakage. He has a wide variety of technical responsibilities, from transducer design and manufacture to data analysis and interpretation. Since 2016, he has supervised three D.Eng. students.